

Land Surface Temperature Estimation from Landsat-9 Thermal Infrared Data Using Ensemble Learning Method Considering the Physical Radiance Transfer Process

Xin Ye ¹, Rongyuan Liu ^{2,*}, Jian Hui ³ and Jian Zhu ¹ 

¹ College of Information and Electrical Engineering, China Agricultural University, Beijing 100083, China

² China Aero Geophysical Survey and Remote Sensing Center for Natural Resources, Beijing 100083, China

³ Hikvision Research Institute, Hangzhou Hikvision Digital Technology Co., Ltd., Hangzhou 310051, China

* Correspondence: liurongyuan@126.com

Abstract: Accurately estimating land surface temperature (LST) is a critical concern in thermal infrared (TIR) remote sensing. According to the thermal radiance transfer equation, the observed data in each channel are coupled with both emissivity and atmospheric parameters in addition to the LST. To solve this ill-posed problem, classical algorithms often require the input of external parameters such as land surface emissivity and atmospheric profiles, which are often difficult to obtain accurately and timely, and this may introduce additional errors and limit the applicability of the LST retrieval algorithms. To reduce the dependence on external parameters, this paper proposes a new algorithm to directly estimate the LST from the top-of-atmosphere brightness temperature in Landsat-9 two-channel TIR data (channels 10 and 11) without external parameters. The proposed algorithm takes full advantage of the adeptness of the ensemble learning method to solve nonlinear problems. It considers the physical radiance transfer process and adds the leaving-ground bright temperature and atmospheric water vapor index to the input feature set. The experimental results show that the new algorithm achieves accurate LST estimation results compared with the ground-measured LST and is consistent with the Landsat-9 LST product. In subsequent work, further studies will be undertaken on developing end-to-end deep learning models, mining more in-depth features between TIR channels, and reducing the effect of spatial heterogeneity on accuracy validation.

Keywords: land surface temperature; thermal infrared; remote sensing; ensemble learning; Landsat-9



Citation: Ye, X.; Liu, R.; Hui, J.; Zhu, J. Land Surface Temperature Estimation from Landsat-9 Thermal Infrared Data Using Ensemble Learning Method Considering the Physical Radiance Transfer Process. *Land* **2023**, *12*, 1287. <https://doi.org/10.3390/land12071287>

Academic Editors: Yuanjian Yang and Luca Salvati

Received: 28 April 2023

Revised: 4 June 2023

Accepted: 13 June 2023

Published: 26 June 2023



Copyright: © 2023 by the authors. Licensee MDPI, Basel, Switzerland. This article is an open access article distributed under the terms and conditions of the Creative Commons Attribution (CC BY) license (<https://creativecommons.org/licenses/by/4.0/>).

1. Introduction

Land surface temperature (LST) is an important parameter affecting the energy and moisture cycle between the land surface and the atmosphere, characterizing the spatial and temporal distribution of the land surface thermal radiance, and plays a crucial role in various fields such as environmental protection, ecology, and agriculture [1]. Thermal infrared (TIR) remote sensing is an efficient approach to obtaining large-scale LST measurements and has received wide attention. LST estimation from TIR remote sensing data is ill-posed since the number of unknowns, including atmospheric parameters (upward radiance, downward radiance, and transmittance) and land surface emissivity for each TIR channel and LST is larger than the number of observed TIR channels [2]. In decades of studies, a variety of LST retrieval algorithms based on the characteristics of different TIR remote sensing data sources have been proposed, including the single-channel (SC) algorithm [3,4], the split-window (SW) algorithm [5–7], the temperature and emissivity separation (TES) algorithm [8–11], and the physics-based day/night (D/N) algorithm [12,13].

The above algorithms simplify the thermal radiance transfer process by setting some assumptions to solve the ill-posed problem, which required accurately and timely obtaining some additional parameters. For example, the SC algorithm requires both land surface emissivity and atmospheric parameters to be known [14,15]. Although the SW algorithm

can eliminate atmospheric effects based on the relationship between adjacent TIR channels, it still requires the input of the land surface emissivity [5,7,16]. The TES and D/N algorithms use the relationship between different channel emissivity values or two observations during daytime and nighttime to estimate the LST and emissivity from the atmospheric corrected TIR data [9,10]. However, accurately obtaining atmospheric parameters and retrieving the land surface emissivity concurrently with satellite observations are often difficult, and the inaccessibility and uncertainty of these external parameters directly reduce the performance and applicability of the above algorithms [17–19]. Therefore, this paper aims to propose a new algorithm for the direct retrieval of the LST from the original bright temperature (BT) observed at the top of the atmosphere without requiring the input of external parameters to enhance the feasibility and stability of LST retrieval under different observation conditions.

Benefitting from the ability to capture nonlinear correlations, machine learning methods, which can provide a direct solution by establishing a link between the input feature set to the output results, have been applied for parameter retrieval from TIR remote sensing data [20], including LST estimation from multiple-channel TIR data [21,22], LST residual optimization from SW algorithm results [23], and the simultaneous retrieval of land surface and atmospheric parameters from TIR hyperspectral data [24–26]. Ensemble learning methods, which can learn multiple hypotheses to solve a problem together by combining various weak learning models, including bagging, boosting, and stacking techniques, have demonstrated the ability to represent complex physical processes well and have been applied to remote sensing applications with promising results, such as mapping natural hazards, predicting crop yields, and spatial downscaling [20,27,28], and they can improve accuracy and reduce overfitting by learning multiple hypotheses from training datasets [29]. In this paper, the ensemble learning method was introduced into LST retrieval to capitalize on its advantages to optimize the performance of the results. In addition, two physical-based new features representing land surface and atmospheric conditions, namely, the leaving-ground BT and water vapor index (WVI), were developed from the thermal radiance transfer equation using the top-of-atmosphere BT [30], which, together with the top-of-atmosphere BT form the input feature, was set to improve the accuracy further.

The proposed physical-based ensemble learning LST estimation algorithm was implemented based on the latest Landsat-9 two-channel TIR data, and its effectiveness was illustrated in the experimental results using the simulation dataset and the observed remote sensing images. This paper is organized as follows: Section 2 gives the TIR simulation dataset and the ensemble learning method. Section 3 describes the performance of the LST estimation algorithm, the Landsat-9 image application, and accuracy verification results. Sections 4 and 5 illustrate the discussion and conclusions separately.

2. Data and Methods

Figure 1 shows the flowchart of the proposed algorithm in this study, which includes three steps: (1) TIR dataset simulation, (2) LST estimation model training, and (3) accuracy verification. First, using global atmospheric profiles and an emissivity library, the MODTRAN model was driven to obtain the simulated Landsat-9 TIR dataset under different land surface and atmospheric conditions. Subsequently, the physics-based features, including TOA BT, leaving-ground BT, and WVI, were developed to train the GBM model for LST estimation. Finally, the LST estimation model was applied to authentic Landsat-9 TIR images to obtain the LST estimation results and validated using ground measurement data and Landsat-9 LST products.

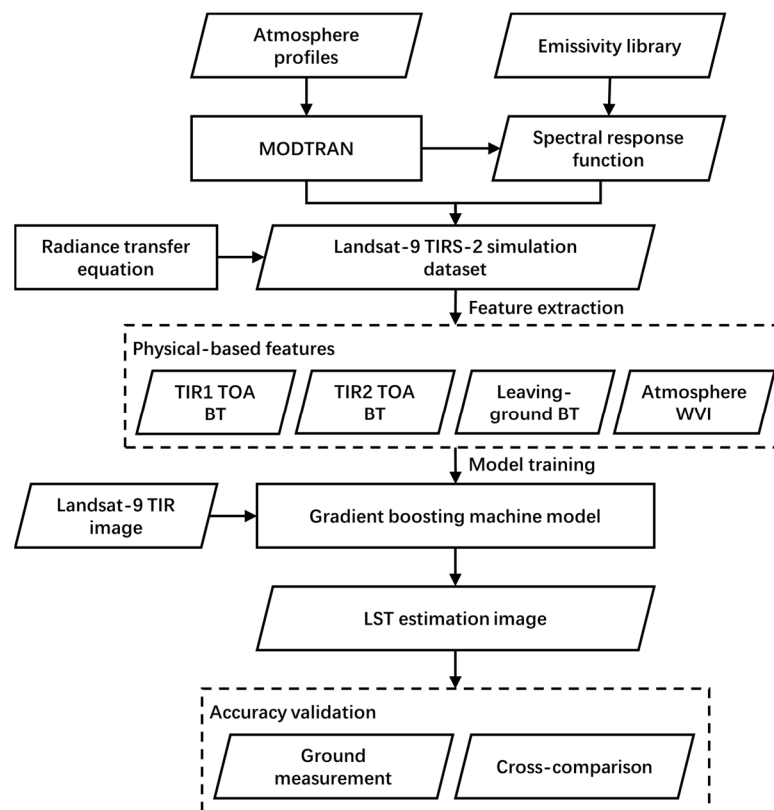


Figure 1. The flowchart of the proposed LST estimation algorithm.

2.1. TIR Simulation Dataset

The Landsat-9 satellite was launched on 27 September 2021, carrying the latest TIR Sensor-2 (TIRS-2), which is capable of acquiring TIR remote sensing images at a 100 m spatial resolution in 2 channels [31,32]. The spectral response functions of the Landsat-9 TIRS-2 data are shown in Figure 2. The spectral ranges of the 2 TIR channels are 10.45–11.20 μm and 11.58–12.50 μm . The Landsat-9 TIR simulation dataset for different atmospheric and land surface conditions was first built using the thermal radiance transfer process to develop the LST estimation algorithm. The radiance observed by the satellite at the top of the atmosphere (L_{TOA}) consists of three components: the land surface emitted radiance, reflected atmospheric downward radiance, and atmospheric upward radiance. The radiance transfer equation is shown in Equation (1):

$$\begin{aligned} L_{TOA} &= [\varepsilon \cdot B(T_s) + (1 - \varepsilon) \cdot L_d] \cdot \tau + L_u \\ &= \varepsilon \cdot B(T_s) \cdot \tau + (1 - \varepsilon) \cdot L_d \cdot \tau + L_u \end{aligned} \quad (1)$$

where ε is the land surface emissivity, T_s is the LST, $B(\cdot)$ is the Planck function, τ is the atmospheric transmittance, and L_d and L_u are the atmospheric downward and upward radiance, respectively. The land surface emitted radiance can be calculated as $\varepsilon \cdot B(T_s) \cdot \tau$, and the reflected atmospheric downward radiance follows Kirchhoff's law.

For atmospheric conditions, 946 global clear-sky atmospheric profiles, including 236 tropical profiles, 258 mid-latitude profiles, and 452 polar profiles, chosen from the Thermodynamic Initial Guess Retrieval (TIGR) database [33] were applied to simulate the atmospheric parameters (L_d , L_u , and τ) during satellite observation by driving the MODerate resolution atmospheric TRANsmission (MODTRAN) model. Moreover, for land surface conditions, an emissivity set including 77 land surface types, which contained 14 vegetation samples, 36 soil samples, 23 rock samples, and 4 water samples, was built from the ASTER [34] and UCSB [35] spectral library. Meanwhile, the LST was set as the sum of the bottom air temperature of each atmospheric profile and a variation of $[-15, 20]$ K (at

5 K intervals). Therefore, a Landsat-9 TIR simulation dataset with 582,736 (946 atmospheric profiles \times 77 land surface samples \times 8 LSTs) sets of data was obtained in this study. It is worth noting that all channel-related parameters were calculated by integrating the spectral response function with the parametric values in the wavelength range of $[\lambda_1, \lambda_2]$, as shown in Equation (2):

$$V_{TIRS-2} = \frac{\int_{\lambda_2}^{\lambda_1} SRF(\lambda) \cdot V(\lambda) d\lambda}{\int_{\lambda_2}^{\lambda_1} SRF(\lambda) d\lambda} \quad (2)$$

where V_{TIRS-2} is the value of the channel-related parameter of the Landsat-9 TIRS-2 data, $SRF(\lambda)$ and $V(\lambda)$ are the spectral response function and parameter value at wavelength λ , respectively.

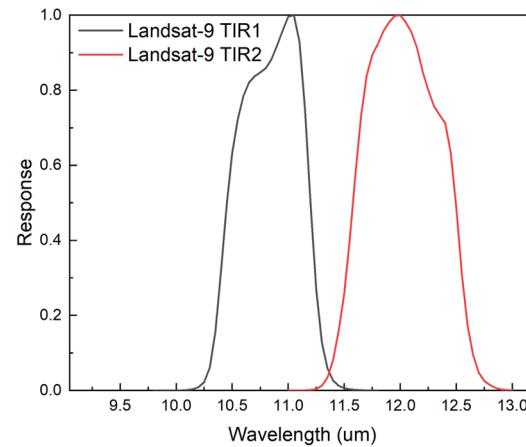


Figure 2. The spectral response functions of the Landsat-9 TIRS-2 data.

2.2. Ensemble Learning Method

In this study, the gradient boosting machine (GBM) method, which is capable of constructing new base learners that are highly correlated with the negative gradient of the loss function associated with the entire ensemble [36], was chosen to estimate the LST due to its demonstrated effectiveness in parameter retrieval from remote sensing data [37,38]. It can be seen from Equation (1) that the TOA BT observed with the satellite couples with both land surface and atmospheric parameters. Therefore, it is reasonable to assume that it would be beneficial to estimate the LST more accurately if the relationship between the BTs of different TIR channels could be used to develop new features that can express the atmospheric conditions, drawing on the ideas of the SC and SW algorithms. In addition to the observed TOA BTs of the two TIR channels, this study extracted two new features, the leaving-ground BT and the atmosphere WVI, that consider the physical process of thermal radiance transfer to represent land surface and atmospheric conditions at the time of observation.

For the land surface condition, an SW-like algorithm was proposed for estimating the leaving-ground BT (T_{LG}) as $B(T_{LG}) = \varepsilon \cdot B(T_s)$, using the top-of-atmosphere (TOA) BTs based on the assumption that the SW terms $(T_i - T_j)$ and $(T_i - T_j)^2$ can reduce the majority of the effect from the reflected atmospheric downward radiance [39], as shown in Equation (3):

$$T_{LG} = a_0 + a_1 T_i + a_2 (T_i - T_j) + a_3 (T_i - T_j)^2 + a_4 \frac{T_i - T_j}{T_i + T_j} \quad (3)$$

where T_i and T_j are the TOA BTs of 2 Landsat-9 TIR channels, and a_n ($n = 0, \dots, 4$) are the empirical coefficients fitted from the simulation dataset. In addition, according to the evaluation of the Landsat-8 TIRS-1 sensor noise [40], Gaussian noise of 0.05 K was added to the BTs to simulate the noise equivalent differential temperature (NE Δ T) of the TIRS-2

sensor. The RMSEs of the leaving-ground BT fits for the 2 TIR channels are 1.142 K (TIR1) and 1.445 K (TIR2), respectively.

Regarding the atmospheric condition, the relationship between column water vapor (CWV) and atmospheric parameters has been investigated [41], and it was found that the polynomial model can be used to fit the relationship without bringing in considerable errors. It can be seen in Figures 3–5 that there is a high correlation between the fit of each parameter, and the first-order linear equation was chosen to ensure the stability of the solution as follows:

$$P_{atm} = k_0 + k_1 \cdot CWV \tag{4}$$

where P_{atm} represents 1 type of atmospheric parameter (upward radiance, downward radiance, or transmittance), and k_n ($n = 0, 1$) represent the fitted empirical coefficients. Substituting the linear model into the thermal radiance transfer equation (Equation (1)) and approximating $(1 - \epsilon) \cdot \tau$ as a constant whose variation can be neglected, the ratio between the leaving-ground radiance ($B(T_{LG_i})$) and the top-of-atmosphere radiance ($B(T_i)$) can be fit using a linear model of a water vapor index that is related to the CWV, as shown in Equation (5):

$$B(T_i) = [B(T_{LG_i}) + b_0] \cdot WVI_i + b_1 \tag{5}$$

where WVI is the atmospheric water vapor index, and the coefficients b_n ($n = 0, 1$) are composed of the empirical coefficients k_n , the fitted empirical coefficients between the CWV and different atmospheric parameters.

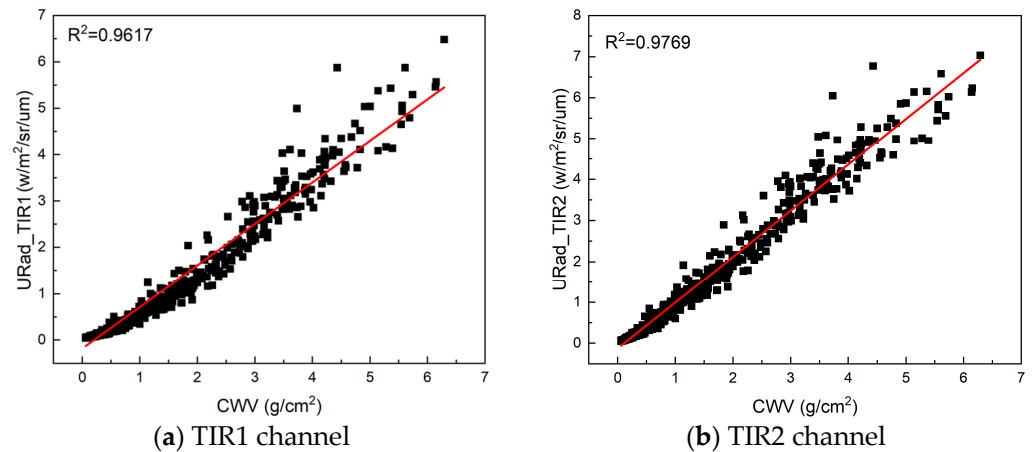


Figure 3. Relationship between CWV and atmospheric upward radiance.

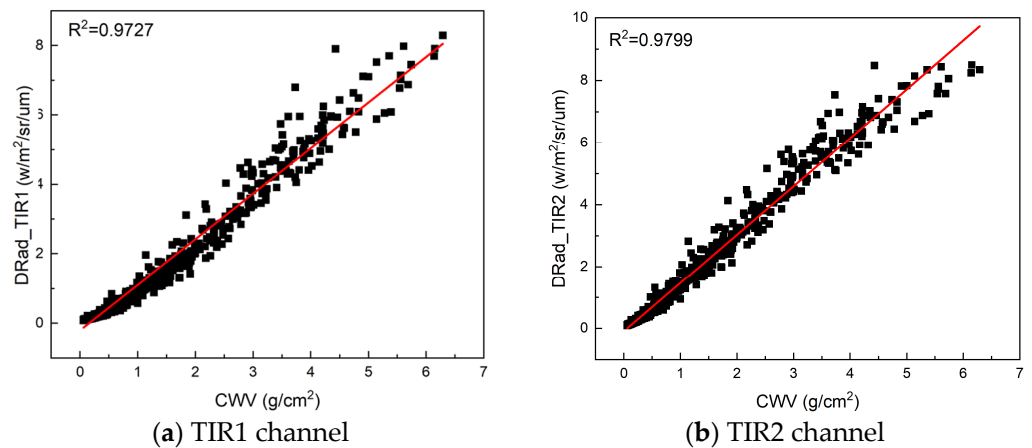


Figure 4. Relationship between CWV and atmospheric downward radiance.

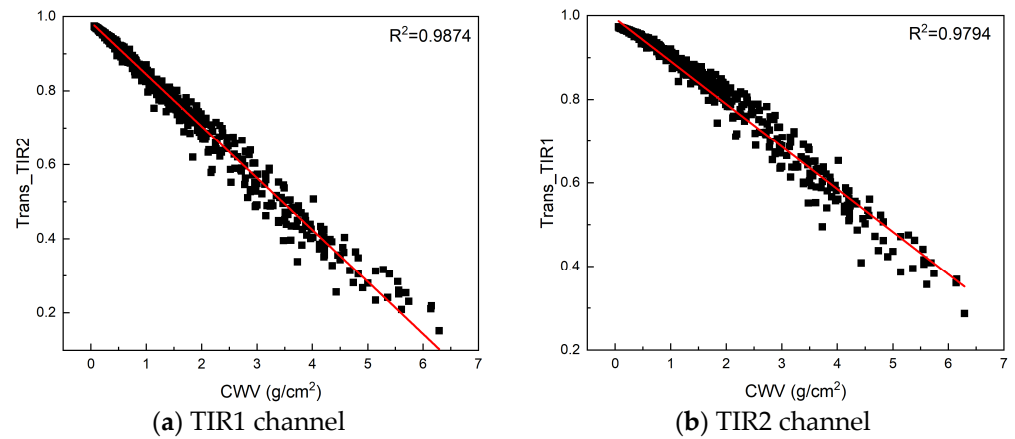


Figure 5. Relationship between CWV and atmospheric transmittance.

In summary, the new algorithm proposed in this study is a direct approach for LST estimation from Landsat-9 TIR remote sensing data using the GBM ensemble learning model. The input training feature set contains the TOA BT, leaving-ground BT, and WVI for each TIR channel. The empirical coefficients of the algorithm can all be fitted from the simulation dataset without relying on external inputs such as emissivity and atmospheric profiles.

3. Experimental Results

3.1. Ensemble Learning Results

To obtain the model capable of estimating the LST, 70% of the simulation dataset was divided into the training dataset to train the ensemble learning model, and the remaining 30% of the data was split into the testing dataset to validate the model performance. The histogram of the LST residual distribution of the LST estimation results using the ensemble learning model is shown in Figure 6a, and the root-mean-square error (RMSE) of the results is 1.496 K with a bias of 0.001 K. Among them, 72.8% of the LST residuals are located in the interval $[-1, 1]$ K and 88.2% in the interval $[-2, 2]$ K. It can be seen that the proposed algorithm has an accurate theoretical performance for LST estimation. The LST estimation results of the ensemble learning model without adding the physical-based features were also evaluated, and the histogram of the residual distribution is shown in Figure 6b. It can be seen that the RMSE grew to 1.679 K, and the percentage of residuals within $[-1, 1]$ K decreased to 66.3%, and that within $[-2, 2]$ K decreased to 85.0%. This indicates that including the leaving-ground BT and WVI effectively improves the estimation accuracy.

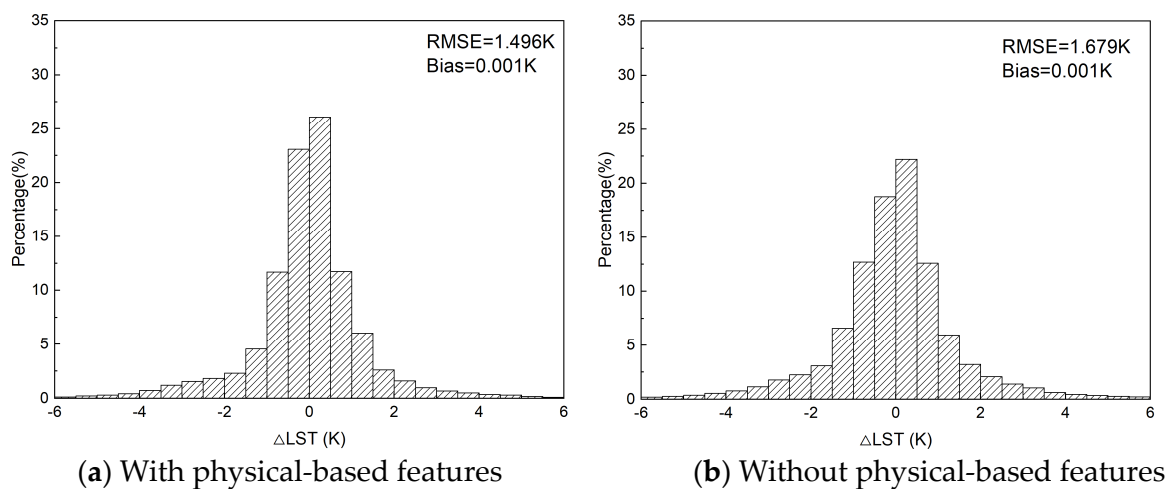


Figure 6. Histogram of LST residuals of the proposed algorithm.

In addition, the accuracy of the model under different regional atmospheric conditions was also evaluated separately. The histogram is shown in Figure 7. As can be seen in the figure, the largest error is 2.160 K for the tropical atmospheric profiles, with residuals in the ranges of $[-1, 1]$ K and $[-2, 2]$ K of 52.1% and 76.5%. The errors for the mid-latitude and polar atmospheric profiles are 1.009 K and 0.638 K, respectively, corresponding to 2 residual proportions of 76.9%/93.9% and 91.6%/97.9%. In contrast, for the model results that do not include the physical-based features, the proportions of the LST residuals located at $[-1, 1]$ K and $[-2, 2]$ K are reduced to 37.8%/66.3%, 70.4%/91.8%, and 86.5%/96.8% for tropical, mid-latitude, and polar atmospheric conditions. Table 1 shows the LST RMSEs of two LST estimation algorithms for different regions, which illustrates the effectiveness of the proposed algorithm.

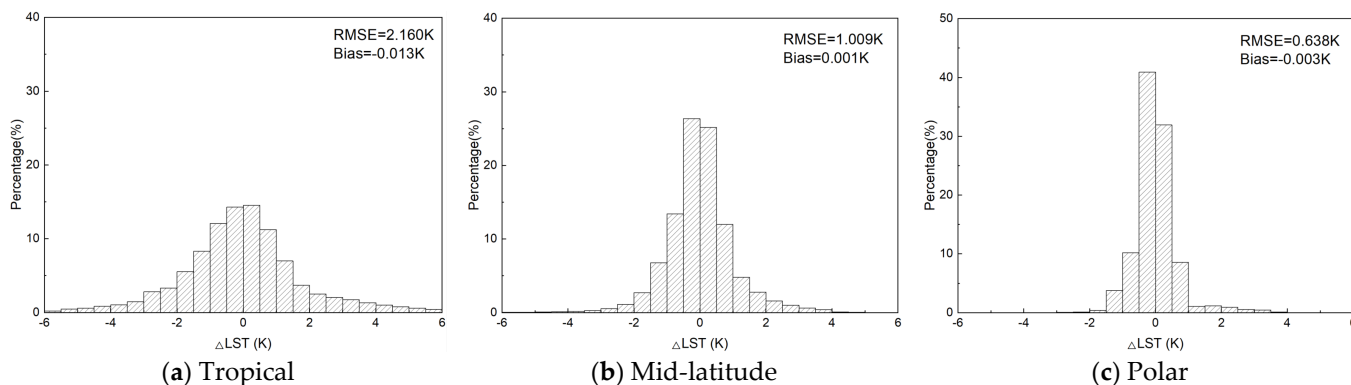


Figure 7. Histogram of LST residuals of the proposed algorithm under different regional atmospheric conditions.

Table 1. LST RMSEs of two LST estimation algorithms for different regions.

| Algorithm | Tropical | Mid-Latitude | Polar | Overall |
|---------------------------------|----------|--------------|-------|---------|
| With physical-based features | 2.160 | 1.009 | 0.638 | 1.496 |
| Without physical-based features | 2.441 | 1.142 | 0.761 | 1.679 |

3.2. LST Estimation Application

The proposed model was applied to the LST estimation of Landsat-9 remote sensing images observed in February 2022, and the LST estimation results for the images located at the GWN site and DRA site of the SURFRAD network [42] are shown in Figures 8a and 9a. A comparison with the fully validated Landsat-9 LST product [32] (Figures 8b and 9b) shows that the value ranges and spatial distributions of both regions are very close. The images (Figures 8c and 9c) and distribution histogram (Figures 8d and 9d) of the LST differences also show no obvious overestimated or underestimated anomalous regions, and the RMSEs of the LST differences in the 2 regions are 0.771 K and 1.289 K. The proportions of the LST differences in $[-1, 1]$ K and $[-2, 2]$ K are 87.1%/97.8% and 50.5%/88.1%, respectively. The comparison results demonstrate that the results of the proposed algorithm were accurate and had high stability.

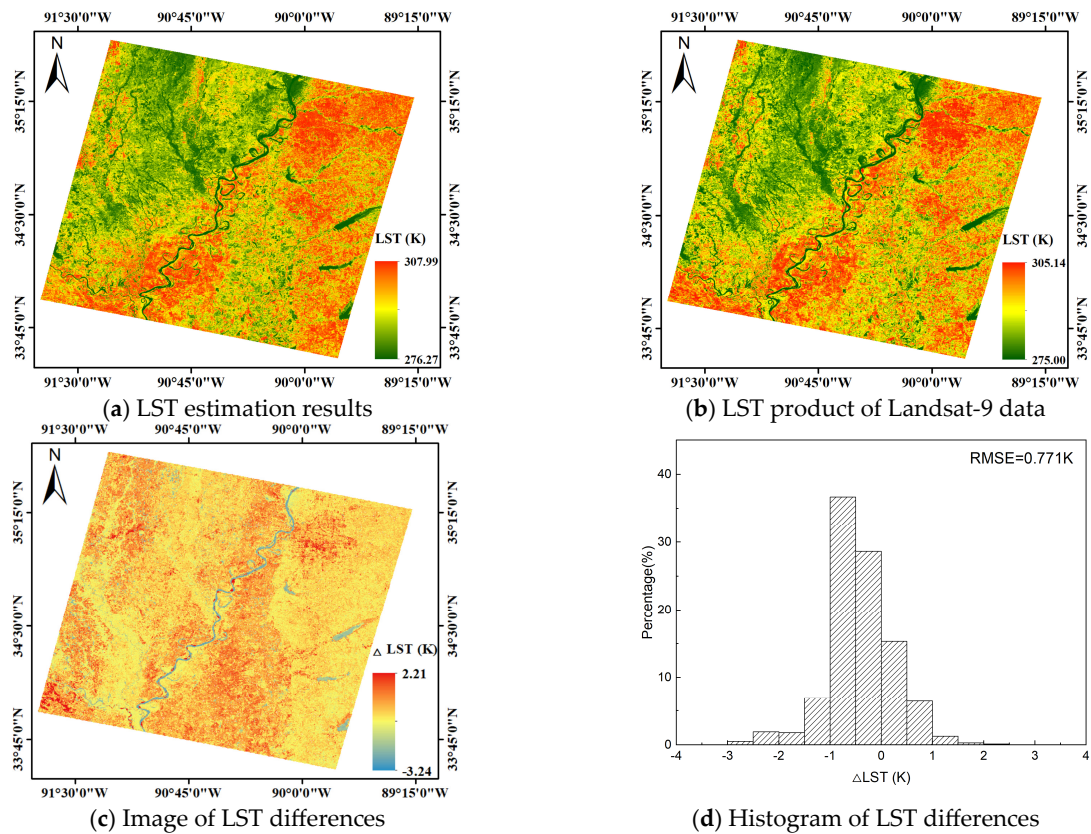


Figure 8. LST estimation results and comparison with the Landsat-9 LST product at the GWN site.

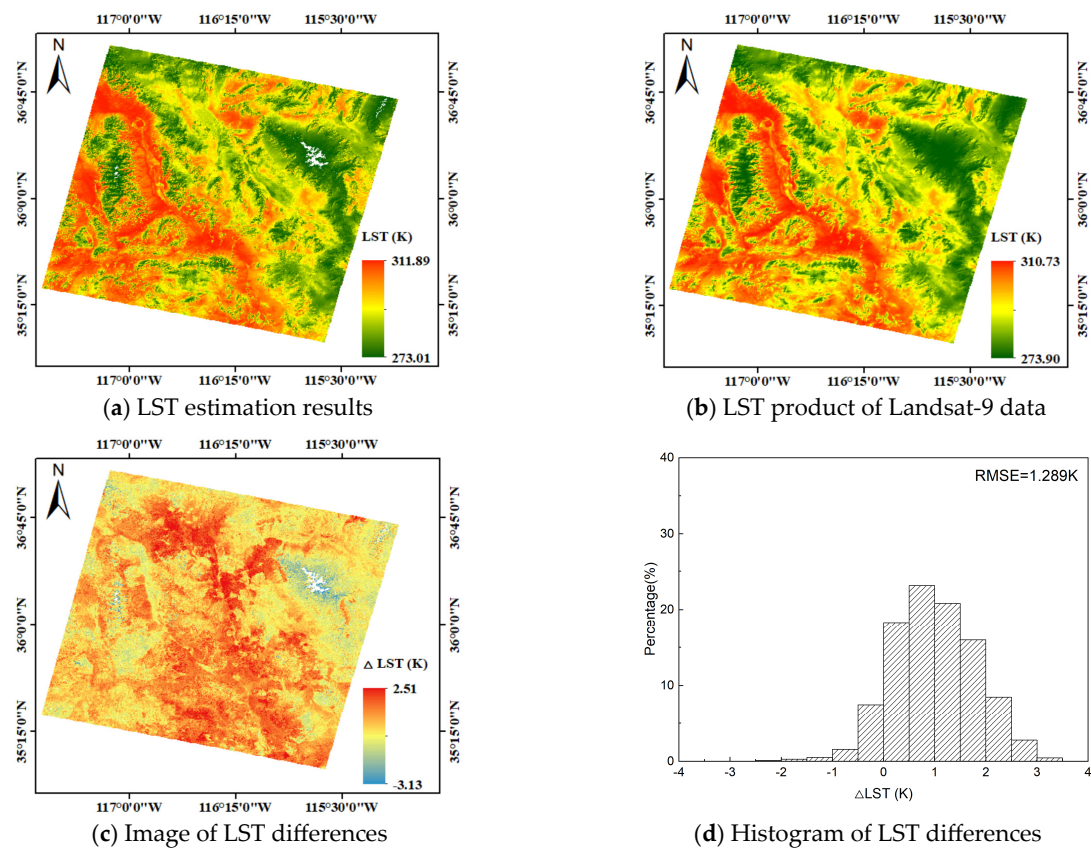


Figure 9. LST estimation results and comparison with the Landsat-9 LST product at the DRA site.

3.3. Accuracy Validation

The Copernicus Ground-Based Observations for Validation (GBOV) [43] ground measurement data and additional Landsat LST products were used to validate the accuracy of the proposed algorithm, and the results are shown in Figure 10a. A total of 44 pairs of ground measurement sites with land cover types, including cropland, grassland, and woodland, were selected, and the RMSE and bias of the LST estimation results using the GBOV data were 2.508 K and -0.465 K with good consistency in the scatter distribution. The estimated LST results were also cross-compared with the values of the Landsat-9 product at the site locations (Figure 10b), and the RMSE and bias between them reached 0.919 K and -0.500 K. The accuracy validation results also indicated that the ensemble learning method considering the physical radiance transfer process could accurately obtain the LST from the Landsat-9 remote sensing images.

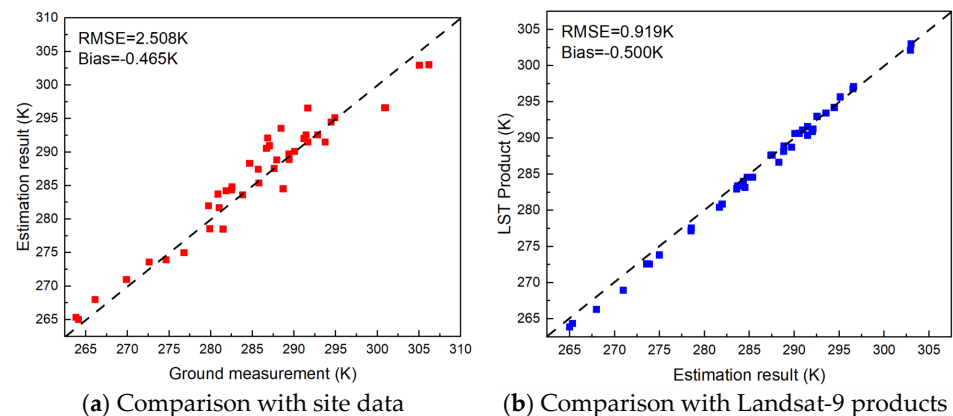


Figure 10. LST ground validation results.

4. Discussion

The results of the LST estimation based on the simulation dataset showed that the new algorithm has the best accuracy in polar regions and the worst in tropical regions, and this decrease in accuracy may be due to the growth in atmospheric CWV. As seen in Figure 5, the increase in CWV causes a reduction in atmospheric transmittance, which reduces the land surface thermal radiance information contained in the TOA BT and leads to an increment in the LST estimation error. Although adding WVI can reduce errors, the trend remains the same. To improve accuracy further, multiple LST estimation models were considered to be trained in different regions and various TOA BT ranges to describe the relationship between the TOA BT and LST more accurately and reduce the interference caused by spatial heterogeneity. Furthermore, an end-to-end deep learning model was considered to automatically extract the deep features between the TOA BT of different channels using neural networks [21,26] instead of manual feature engineering.

The new algorithm was proposed based on the Landsat-9 two-channel TIR data and is theoretically applicable to most current TIR remote sensing data sources. However, for TIR data containing more channels, such as MODIS, ASTER, Gaofen-5, etc., the algorithm using only two channels does not take full advantage of the data. Therefore, the most appropriate TIR channel input for LST estimation can be chosen by comparing the accuracy of LST estimation with different channel combinations. The TES algorithm can also be established using multi-channel TIR data to simultaneously estimate emissivity and the LST by developing the empirical relationship of the maximum–minimum apparent emissivity difference (MMD) [11,39,44]. In addition, there are significant differences in the spatial resolutions of different satellite-based TIR images, ranging from 1 km to 10s of meters. With an increase in spatial resolution, the incorporation of DSM data to express the influence of the three-dimensional structure during the transfer process of thermal radiance from the target pixels would be necessary for a land surface with complex structures such as urban and mountainous areas [45–47].

The accuracy validation results based on ground measurement data show that the new algorithm can accurately estimate LST. It was also found that the estimated LSTs were in better agreement with the Landsat-9 remote sensing products through cross-comparison, which further demonstrated the validity of the proposed algorithm and also illustrated that the direct comparison between the measured point data from ground sites and the area data observed with the satellite may be influenced by the spatial heterogeneity of the land surface. For the Landsat-9 TIR remote sensing image with a 100 m spatial resolution, a pixel may still contain components with multiple land cover types and different LSTs, so the variability introduced by mixed pixels should be addressed. Therefore, spatial sampling methods that consider pixel heterogeneity [48,49] could be brought in to improve the effectiveness of validation.

5. Conclusions

In this study, a new algorithm that can estimate LST accurately without requiring external input parameters was proposed based on the ensemble learning method from Landsat-9 TIR data. The input feature set consists of the observed TOA BT and the derived leaving-ground BT representing land surface conditions and the WVI representing atmospheric conditions. In terms of the ensemble learning models, the GBM was chosen due to its promising performance in remote sensing parameter retrieval and trained using the simulation dataset. The model training results show that the GBM model effectively estimates LST with an overall RMSE of less than 1.50 K, and the inclusion of new physical-based features successfully reduced the error by approximately 0.20 K. The performance of the new algorithm under different atmospheric conditions in various regions was evaluated, and it was found that the accuracy in polar regions was better than that in mid-latitude regions, and the uncertainty in tropical regions was the largest, which was likely due to the increased atmospheric water vapor content. The Landsat-9 LST estimation images were obtained using the proposed algorithm, validated with the GBOV ground measurement data, and cross-compared with Landsat-9 LST products. The accuracy validation results show an RMSE of approximately 2.5 K verified with ground measurement data and good consistency with the spatial distribution and numerical comparison of the remote sensing products. Future work could include developing an end-to-end deep learning model to automatically extract deep features, extending the proposed algorithm to more TIR data, and introducing new sampling strategies and mixed pixel decomposition to improve the reliability of validation.

Author Contributions: Conceptualization, X.Y., R.L. and J.H.; methodology, X.Y., R.L. and J.H.; validation, X.Y., R.L. and J.Z.; formal analysis, X.Y., R.L. and J.H.; investigation, X.Y. and R.L.; resources, X.Y. and R.L.; data curation, X.Y., R.L. and J.H.; writing—original draft preparation, X.Y., R.L. and J.H.; writing—review and editing, X.Y. and R.L.; visualization, X.Y. and J.Z.; supervision, X.Y. and R.L.; project administration, R.L. All authors have read and agreed to the published version of the manuscript.

Funding: This research received no external funding.

Data Availability Statement: The Landsat-9 images supporting the reported results can be found and downloaded at <https://earthexplorer.usgs.gov/> (accessed on 24 April 2023).

Acknowledgments: The authors are grateful to GBOV for providing the ground-measured land surface temperature data.

Conflicts of Interest: The authors declare no conflict of interest.

References

1. Li, Z.L.; Wu, H.; Duan, S.B.; Zhao, W.; Ren, H.; Liu, X.; Leng, P.; Tang, R.; Ye, X.; Zhu, J.; et al. Satellite remote sensing of global land surface temperature: Definition, methods, products, and applications. *Rev. Geophys.* **2023**, *61*, e2022RG000777. [[CrossRef](#)]
2. Li, Z.-L.; Tang, B.-H.; Wu, H.; Ren, H.; Yan, G.; Wan, Z.; Trigo, I.F.; Sobrino, J.A. Satellite-derived land surface temperature: Current status and perspectives. *Remote Sens. Environ.* **2013**, *131*, 14–37. [[CrossRef](#)]

3. Jimenez-Munoz, J.C.; Cristobal, J.; Sobrino, J.A.; Soria, G.; Ninyerola, M.; Pons, X.; Pons, X. Revision of the Single-Channel Algorithm for Land Surface Temperature Retrieval From Landsat Thermal-Infrared Data. *IEEE Trans. Geosci. Remote Sens.* **2009**, *47*, 339–349. [[CrossRef](#)]
4. Qin, Z.; Karnieli, A.; Berliner, P. A mono-window algorithm for retrieving land surface temperature from Landsat TM data and its application to the Israel-Egypt border region. *Int. J. Remote Sens.* **2001**, *22*, 3719–3746. [[CrossRef](#)]
5. Wan, Z. New refinements and validation of the collection-6 MODIS land-surface temperature/emissivity product. *Remote Sens. Environ.* **2014**, *140*, 36–45. [[CrossRef](#)]
6. Du, C.; Ren, H.; Qin, Q.; Meng, J.; Zhao, S. A Practical Split-Window Algorithm for Estimating Land Surface Temperature from Landsat 8 Data. *Remote Sens.* **2015**, *7*, 647–665. [[CrossRef](#)]
7. Ye, X.; Ren, H.; Liu, R.; Qin, Q.; Liu, Y.; Dong, J. Land Surface Temperature Estimate From Chinese Gaofen-5 Satellite Data Using Split-Window Algorithm. *IEEE Trans. Geosci. Remote Sens.* **2017**, *55*, 5877–5888. [[CrossRef](#)]
8. Jiménez-Muñoz, J.C.; Sobrino, J.A.; Mattar, C.; Hulley, G.; Gottsche, F.-M. Temperature and emissivity separation from MSG/SEVIRI data. *IEEE Trans. Geosci. Remote Sens.* **2014**, *52*, 5937–5951. [[CrossRef](#)]
9. Gillespie, A.; Rokugawa, S.; Matsunaga, T.; Cothem, J.S.; Hook, S.; Kahle, A.B. A Temperature and Emissivity Separation Algorithm for Advanced Spaceborne Thermal Emission and Reflection Radiometer (ASTER) Images. *IEEE Trans. Geosci. Remote Sens.* **1998**, *36*, 1113–1126. [[CrossRef](#)]
10. Gillespie, A.R.; Abbott, E.A.; Gilson, L.; Hulley, G.; Jiménez-Muñoz, J.-C.; Sobrino, J.A. Residual errors in ASTER temperature and emissivity standard products AST08 and AST05. *Remote Sens. Environ.* **2011**, *115*, 3681–3694. [[CrossRef](#)]
11. Ren, H.; Ye, X.; Liu, R.; Dong, J.; Qin, Q. Improving land surface temperature and emissivity retrieval from the Chinese Gaofen-5 satellite using a hybrid algorithm. *IEEE Trans. Geosci. Remote Sens.* **2018**, *56*, 1080–1090. [[CrossRef](#)]
12. Zhao-Liang, L.; François, P.; Renhua, Z. A physically based algorithm for land surface emissivity retrieval from combined mid-infrared and thermal infrared data. *Sci. China Ser. E Technol. Sci.* **2000**, *43*, 23–33.
13. Wan, Z.; Li, Z.-L. A Physics-Based Algorithm for Retrieving Land-Surface Emissivity and Temperature from EOS/MODIS Data. *IEEE Trans. Geosci. Remote Sens.* **1997**, *35*, 980–996. [[CrossRef](#)]
14. Jiménez-Muñoz, J.C.; Sobrino, J.A. A generalized single-channel method for retrieving land surface temperature from remote sensing data. *J. Geophys. Res. Atmos.* **2003**, *108*. [[CrossRef](#)]
15. Jimenez-Munoz, J.C.; Sobrino, J.A. A Single-Channel Algorithm for Land-Surface Temperature Retrieval From ASTER Data. *IEEE Geosci. Remote Sens. Lett.* **2010**, *7*, 176–179. [[CrossRef](#)]
16. Becker, F.; Li, Z.-L. Towards a local split window method over land surfaces. *Int. J. Remote Sens.* **1990**, *11*, 369–393. [[CrossRef](#)]
17. Yu, X.; Guo, X.; Wu, Z. Land Surface Temperature Retrieval from Landsat 8 TIRS—Comparison between Radiative Transfer Equation-Based Method, Split Window Algorithm and Single Channel Method. *Remote Sens.* **2014**, *6*, 9829–9852. [[CrossRef](#)]
18. Malakar, N.K.; Hulley, G.C. A water vapor scaling model for improved land surface temperature and emissivity separation of MODIS thermal infrared data. *Remote Sens. Environ.* **2016**, *182*, 252–264. [[CrossRef](#)]
19. Li, Z.-L.; Wu, H.; Wang, N.; Qiu, S.; Sobrino, J.A.; Wan, Z.; Tang, B.-H.; Yan, G. Land surface emissivity retrieval from satellite data. *Int. J. Remote Sens.* **2013**, *34*, 3084–3127. [[CrossRef](#)]
20. Zhang, Y.; Liu, J.; Shen, W. A Review of Ensemble Learning Algorithms Used in Remote Sensing Applications. *Appl. Sci.* **2022**, *12*, 8654. [[CrossRef](#)]
21. Wang, H.; Mao, K.; Yuan, Z.; Shi, J.; Cao, M.; Qin, Z.; Duan, S.; Tang, B. A method for land surface temperature retrieval based on model-data-knowledge-driven and deep learning. *Remote Sens. Environ.* **2021**, *265*, 112665. [[CrossRef](#)]
22. Bai, Y.; Wong, M.; Shi, W.-Z.; Wu, L.-X.; Qin, K. Advancing of Land Surface Temperature Retrieval Using Extreme Learning Machine and Spatio-Temporal Adaptive Data Fusion Algorithm. *Remote Sens.* **2015**, *7*, 4424–4441. [[CrossRef](#)]
23. Ye, X.; Ren, H.; Liang, Y.; Zhu, J.; Guo, J.; Nie, J.; Zeng, H.; Zhao, Y.; Qian, Y. Cross-calibration of Chinese Gaofen-5 thermal infrared images and its improvement on land surface temperature retrieval. *Int. J. Appl. Earth Obs. Geoinf.* **2021**, *101*, 102357. [[CrossRef](#)]
24. Wang, N.; Li, Z.-L.; Tang, B.-H.; Zeng, F.; Li, C. Retrieval of atmospheric and land surface parameters from satellite-based thermal infrared hyperspectral data using a neural network technique. *Int. J. Remote Sens.* **2012**, *34*, 3485–3502. [[CrossRef](#)]
25. Ren, H.; Ye, X.; Nie, J.; Meng, J.; Fan, W.; Qin, Q.; Liang, Y.; Liu, H. Retrieval of Land Surface Temperature, Emissivity, and Atmospheric Parameters From Hyperspectral Thermal Infrared Image Using a Feature-Band Linear-Format Hybrid Algorithm. *IEEE Trans. Geosci. Remote Sens.* **2022**, *60*, 1–15. [[CrossRef](#)]
26. Ye, X.; Ren, H.; Nie, J.; Hui, J.; Jiang, C.; Zhu, J.; Fan, W.; Qian, Y.; Liang, Y. Simultaneous Estimation of Land Surface and Atmospheric Parameters From Thermal Hyperspectral Data Using a LSTM-CNN Combined Deep Neural Network. *IEEE Geosci. Remote Sens. Lett.* **2022**, *19*, 1–5. [[CrossRef](#)]
27. Thongsuwan, S.; Jaiyen, S.; Padcharoen, A.; Agarwal, P. ConvXGB: A new deep learning model for classification problems based on CNN and XGBoost. *Nucl. Eng. Technol.* **2021**, *53*, 522–531. [[CrossRef](#)]
28. Zamani Joharestani, M.; Cao, C.; Ni, X.; Bashir, B.; Talebiesfandarani, S. PM2.5 Prediction Based on Random Forest, XGBoost, and Deep Learning Using Multisource Remote Sensing Data. *Atmosphere* **2019**, *10*, 373. [[CrossRef](#)]
29. Mendes-Moreira, J.; Soares, C.; Jorge, A.M.; Sousa, J.F.D. Ensemble approaches for regression. *ACM Comput. Surv.* **2012**, *45*, 1–40. [[CrossRef](#)]

30. Cai, J.; Luo, J.; Wang, S.; Yang, S. Feature selection in machine learning: A new perspective. *Neurocomputing* **2018**, *300*, 70–79. [[CrossRef](#)]
31. Masek, J.G.; Wulder, M.A.; Markham, B.; McCorkel, J.; Crawford, C.J.; Storey, J.; Jenstrom, D.T. Landsat 9: Empowering open science and applications through continuity. *Remote Sens. Environ.* **2020**, *248*, 111968. [[CrossRef](#)]
32. USGS. *Landsat 8-9 Calibration and Validation Algorithm Description Document*; USGS: Reston, VA, USA, 2021.
33. Chevallier, F.; Chérury, F.; Scott, N.A.; Chédin, A. A Neural Network Approach for a Fast and Accurate Computation of a Longwave Radiative Budget. *J. Appl. Meteorol.* **1998**, *37*, 1385–1397. [[CrossRef](#)]
34. Baldrige, A.M.; Hook, S.J.; Grove, C.I.; Rivera, G. The ASTER spectral library version 2.0. *Remote Sens. Environ.* **2009**, *113*, 711–715. [[CrossRef](#)]
35. Williams, C.S.; Wan, Z.; Zhang, Y.; Feng, Y. Thermal Infrared (3–14 μm) bidirectional reflectance measurements of sands and soils. *Remote Sens. Environ.* **1997**, *60*, 101–109. [[CrossRef](#)]
36. Natekin, A.; Knoll, A. Gradient boosting machines, a tutorial. *Front. Neurobot.* **2013**, *7*, 21. [[CrossRef](#)] [[PubMed](#)]
37. Abdul Gafoor, F.; Al-Shehhi, M.R.; Cho, C.-S.; Ghedira, H. Gradient Boosting and Linear Regression for Estimating Coastal Bathymetry Based on Sentinel-2 Images. *Remote Sens.* **2022**, *14*, 5037. [[CrossRef](#)]
38. Park, J.; Moon, J.; Jung, S.; Hwang, E. Multistep-Ahead Solar Radiation Forecasting Scheme Based on the Light Gradient Boosting Machine: A Case Study of Jeju Island. *Remote Sens.* **2020**, *12*, 2271. [[CrossRef](#)]
39. Ren, H.; Dong, J.; Liu, R.; Zheng, Y.; Guo, J.; Chen, S.; Nie, J.; Zhao, Y. New hybrid algorithm for land surface temperature retrieval from multiple-band thermal infrared image without atmospheric and emissivity data inputs. *Int. J. Digital Earth* **2020**, *13*, 1430–1453. [[CrossRef](#)]
40. Montanaro, M.; Levy, R.; Markham, B. On-Orbit Radiometric Performance of the Landsat 8 Thermal Infrared Sensor. *Remote Sens.* **2014**, *6*, 11753–11769. [[CrossRef](#)]
41. Wang, M.; Zhang, Z.; Hu, T.; Liu, X. A Practical Single-Channel Algorithm for Land Surface Temperature Retrieval: Application to Landsat series data. *J. Geophys. Res. Atmos.* **2019**, *124*, 299–316. [[CrossRef](#)]
42. Augustine, J.A.; DeLuisi, J.J.; Long, C.N. SURFRAD—A national surface radiation budget network for atmospheric research. *Bull. Am. Meteorol. Soc.* **2000**, *81*, 2341–2357. [[CrossRef](#)]
43. Dodd, E.; Ghent, D. Ground-Based Observations for validation (GBOV) of Copernicus Global Land Products—Algorithm Theoretical Basic Document Land Surface Temperature (LP7). 2019. Available online: https://gbov.acri.fr/public/docs/products/2020-10/GBOV-ATBD-LP7_v2.0-LST.pdf (accessed on 21 September 2020).
44. Zheng, X.; Li, Z.-L.; Wang, T.; Huang, H.; Nerry, F. Determination of global land surface temperature using data from only five selected thermal infrared channels: Method extension and accuracy assessment. *Remote Sens. Environ.* **2022**, *268*, 112774. [[CrossRef](#)]
45. Ye, X.; Ren, H.; Wang, P.; Zhu, J.; Zhu, J. Thermal Infrared Radiance Transfer Modeling of the Urban Landscape at Ultrahigh Spatial Resolution. *IEEE Geosci. Remote Sens. Lett.* **2023**, *20*, 1–5. [[CrossRef](#)]
46. Chen, S.; Ren, H.; Ye, X.; Dong, J.; Zheng, Y. Geometry and adjacency effects in urban land surface temperature retrieval from high-spatial-resolution thermal infrared images. *Remote Sens. Environ.* **2021**, *262*, 112518. [[CrossRef](#)]
47. Zhu, X.; Duan, S.; Li, Z.-L.; Zhao, W.; Wu, H.; Leng, P.; Gao, M.; Zhou, X. Retrieval of land surface temperature with topographic effect correction from Landsat 8 thermal infrared data in mountainous areas. *IEEE Trans. Geosci. Remote Sens.* **2020**, *59*, 6674–6687. [[CrossRef](#)]
48. Duan, S.-B.; Li, Z.-L.; Li, H.; Götsche, F.-M.; Wu, H.; Zhao, W.; Leng, P.; Zhang, X.; Coll, C. Validation of Collection 6 MODIS land surface temperature product using in situ measurements. *Remote Sens. Environ.* **2019**, *225*, 16–29. [[CrossRef](#)]
49. Li, J.; Wu, H.; Li, Z.-L. An optimal sampling method for multi-temporal land surface temperature validation over heterogeneous surfaces. *ISPRS J. Photogramm. Remote Sens.* **2020**, *169*, 29–43. [[CrossRef](#)]

Disclaimer/Publisher’s Note: The statements, opinions and data contained in all publications are solely those of the individual author(s) and contributor(s) and not of MDPI and/or the editor(s). MDPI and/or the editor(s) disclaim responsibility for any injury to people or property resulting from any ideas, methods, instructions or products referred to in the content.